ADVANCED FUNCTIONAL MATERIALS
www.afm-journal.de

CO_2 Reduction on Copper-Nitrogen-Doped Carbon Catalysts Tuned by Pulsed Potential Electrolysis: Effect of Pulse Potential

*Dorottya Hursán, Janis Timoshenko, Andrea Martini, Hyo Sang Jeon, Eduardo Ortega, Martina Rüscher, Arno Bergmann, Aram Yoon, Uta Hejral, Antonia Herzog, Clara Rettenmaier, Felix T. Haase, Philipp Grosse, and Beatriz Roldan Cuenya**

Pulsed electrolysis attracts attention as a simple tool for tuning the structure and properties in many electrocatalytic systems. Here, pulsed reaction protocols are used to control the structure and selectivity of copper and nitrogen co-doped carbon (Cu-N-C) catalysts, employed for electrocatalytic CO_2 reduction reaction (CO_2RR). Specifically, while this catalyst is mostly selective for hydrogen during potentiostatic reduction, as high as 82% Faradaic efficiency for CO_2RR products is reached by optimizing the pulse parameters. It is found that the product distribution depends strongly on the values of both the anodic and cathodic potentials, and the pulse parameter ranges for preferential CO, CH_4, and C_2H_4 formation were identified. By performing detailed in situ and *operando* spectroscopic analysis, it is found that i) pulsing creates a favorable microenvironment for CO_2RR by reducing the surface H-coverage on the N-doped carbon support, and ii) the dynamic evolution of the Cu active sites directs the selectivity toward hydrocarbons (CH_4, C_2H_4). The periodic application of increasingly more anodic potentials results in more efficient redispersion of the metallic Cu clusters that are formed under cathodic potential. The C_1/C_{2+} selectivity ratio depends on the fraction of the stabilized Cu single atoms and the size of the Cu particles formed under working conditions.

1. Introduction

The steadily decreasing cost of renewable electricity is now unlocking the possibility of developing innovative technologies that can directly convert this intermittent energy into valuable fuels and chemicals. Electrochemical carbon dioxide reduction (CO_2RR) is a promising way to reach this goal, with the added value of using a greenhouse gas as feedstock, thus recycling waste CO_2 to reach a circular carbon economy. Notable progress has been made in recent years, both in terms of fundamental understanding of the CO_2RR reaction,[1] as well as catalyst design.[2] With the notable progress made in the continuous-flow electrolyzer technology, industrial implementation is becoming a reality.[3,4] Nonetheless, despite the massive advancement of the field, several challenges must be tackled to fulfil high selectivity, current density, energy efficiency, and long-term stability at the same time.

High selectivity (>90%) under practically-relevant conditions has so far only been reached for C_1 products (CO, HCOOH), while the selective production of high-value multicarbon products directly from CO_2, such as ethylene or ethanol, is still challenging.[5–7] This is tightly related to the fact that Cu is the only metal capable of producing C_{2+} products with reasonable rates.[8] Its selectivity toward a specific product, however, is generally low, necessitating downstream product separation, imposing extra costs.[9] Therefore, steering the selectivity of Cu catalysts is at the forefront of CO_2RR research. Varying the applied potential is the most straightforward way to control selectivity;[10] however, it is inherently coupled to the rate of reaction (current) and the energy efficiency (overpotential). Accordingly, several strategies have been employed to increase the Faradaic efficiency (FE) for a given product, while maintaining high current density at low overpotential. These include surface faceting,[11,12] nanostructuring,[13] alloying,[14] electrolyte engineering[15,16] or improving CO_2 transport by the reactor design.[3] Another versatile, yet simple method is the pulsed CO_2RR (p-CO_2RR),[17–24] where a unique reaction environment is created by the periodic interruption of the reduction reaction through the application of a more positive (anodic) potential.

D. Hursán, J. Timoshenko, A. Martini, H. S. Jeon, E. Ortega, M. Rüscher, A. Bergmann, A. Yoon, U. Hejral, A. Herzog, C. Rettenmaier, F. T. Haase, P. Grosse, B. Roldan Cuenya
Department of Interface Science
Fritz-Haber Institute of the Max Planck Society
14195 Berlin, Germany
E-mail: roldan@fhi-berlin.mpg.de

The ORCID identification number(s) for the author(s) of this article can be found under https://doi.org/10.1002/adfm.202510827

DOI: 10.1002/adfm.202510827

Although the concept of pulsed electrolysis dates back to the beginning of the 19th century, and today is widely applied in the field of electrochemical metal deposition (i.e., pulse plating),[25] only recently it has gained increased interest in the context of CO_2 reduction. Alternating between the cathodic (E_c) and anodic (E_a) potential introduces changes on the catalyst surface (e.g., oxidation, restructuring, roughening, dissolution), in the electric double layer (modulation of the surface coverage and intermediate binding energies), and in the electrolyte (reactant replenishing).[23] Since these processes occur on different time scales, not only the applied potentials[26] but also the choice of the pulse length[17,27] and symmetry[28] present a largely untapped opportunity to enhance reaction selectivity or improve catalyst durability. Taking advantage of these, *p*-CO_2RR is widely studied nowadays both from a fundamental and an application-oriented perspective. For instance, potential pulsing has been shown to enhance the stability of the CO_2RR on Cu by mitigating catalyst poisoning.[19,20] Furthermore, depending on the anodic potential and pulse length, suppression of H_2 evolution (HER) and an increase in hydrocarbon selectivity were also observed. These were attributed to i) enhanced CO accumulation and hydrogen desorption on the catalyst surface,[18,22] ii) local pH-variations,[17] changes in catalyst iii) morphology,[21] iv) oxidation state[21] or v) relative adsorbate coverage.[29] These processes occur in parallel during *p*-CO_2RR, and the observed selectivity shift results from the interplay of such dynamic changes at the interface, making it challenging to decouple the underlying mechanisms. Nonetheless, *p*-CO_2RR could potentially offer a way to selectively produce different products on the same catalyst, thus allowing for easy adjustment to market needs. Furthermore, control over the catalyst structure through pulsing can bypass time-consuming synthesis work, accelerating the identification of structure-performance correlations. Recently, the applicability of *p*-CO_2RR was demonstrated under practically relevant conditions (i.e., in flow cells) too, showcasing the beneficial effect of this operating mode in real-world applications.[26,30]

Existing studies in the field of *p*-CO_2RR have predominantly focused on metals,[31] particularly Cu electrodes.[23] Recently, however, metal-nitrogen-doped carbons (M-N-C) emerged as promising catalysts for CO_2RR.[32–35] These materials differ fundamentally from the bulk or even nanostructured metal electrodes and, as a result, may exhibit markedly different selectivity compared to their metallic counterparts.[10,34] In these systems, the active sites are considered to include both singly dispersed metal sites,[34] and the nitrogen dopants distributed in a conductive carbon matrix.[36] The Cu-N-C catalyst system is particularly interesting as several studies have demonstrated the formation of metallic Cu clusters during CO_2RR under potentiostatic conditions.[32,37–39] Strikingly, this process is completely[40]reversible, and after exposure to air or oxidizing potentials, the Cu clusters disappear as Cu species disperse again. Although the exact mechanism is still under debate, several factors were suggested to play a role in the intriguing trends observed for these materials under anodic potential conditions. These include the strength of the metal-ligand (N/O) bond in the as prepared catalysts,[39] interactions between the formed clusters and the N-C support and/or electrolyte and reaction intermediate species, as well as the thermodynamic instability of the oxide clusters.[40–42] This surprising feature makes Cu-N-C catalysts particularly attractive candidates for *p*-CO_2RR studies. In our previous study, we demonstrated that by tuning the duration of applied potential pulses, we can induce significant changes in the Cu-N-C catalyst selectivity, reversibly switching from predominantly H_2-producing to CH_4- and to CO-producing regimes.[24] We attributed this remarkable behavior of Cu-N-C catalyst to the periodic formation and redispersion of metallic Cu clusters and particles under pulsed CO_2RR.

Nonetheless, many details of this phenomenon remain unclear. In particular, the dependency of this process on the specific values of applied potential has not yet been investigated. Furthermore, potential pulsing can introduce changes not only in the metal sites (e.g., cluster formation, oxidation, leaching), but also in the nitrogen dopants and the carbon structure, which was not studied previously. These effects could provide further possibilities to steer the catalytic functionality of the catalyst on demand.

In this contribution, we build upon our previous work to further demonstrate the tunability of the CO_2RR selectivity by the optimization of the potential pulse parameters employed, with a particular focus on the values of the cathodic and anodic potential. By changing the potential values, the coordination number and the fraction of singly dispersed Cu species can be controlled, resulting in striking selectivity changes. We also contribute to a more in-depth understanding of this complex Cu-N-C material system dynamics via a thorough characterization, including quasi in situ X-ray photoelectron spectroscopy (XPS) measurements, time-resolved operando X-ray absorption fine structure (XAFS) spectroscopy in quick XAFS (QXAFS) mode, operando valence-to-core X-ray emission experiments (vtc-XES), and high-energy resolution fluorescence detected (HERFD) XAS. In particular, the excellent time-resolution achieved in the QXAFS mode (≈1 s per spectrum) allowed us to track the changes in the oxidation state and coordination environment of the copper active sites during individual potential pulses, and, thus, to directly interrogate the catalyst's response to dynamic reaction conditions.

2. Results and Discussion

2.1. Catalytic Properties under Potentiostatic and Pulsed Reaction Conditions

The Cu-N-C catalysts were synthesized by an impregnation-calcination method, described in our previous work.[39] The successful metal-doping of the N-doped carbon support was confirmed by XPS, and inductively coupled plasma mass spectrometry (ICP-MS) measurements (Table S1, Figures S3 and S4, Supporting Information). Besides Cu, the material contained Zn dopants in comparable amounts, remaining from the ZIF-8 precursor. The Cu 2p XPS region (Figure S4, Supporting Information) was dominated by Cu^{2+}, with only a minor contribution from Cu^+ or Cu^0 species. XRD analysis (Figure S3, Supporting Information) and transmission electron microscopic (TEM) imaging (Figure S3, Supporting Information) revealed the absence of metallic nanoparticles in the amorphous carbon matrix for the as-prepared catalyst. High-resolution high-angle annular dark field scanning transmission electron microscopy images (HAADF-STEM), however, clearly showed that heavier elements (i.e., Cu and Zn) are present as single atoms in the as-prepared samples. These measurements, supported by the X-ray

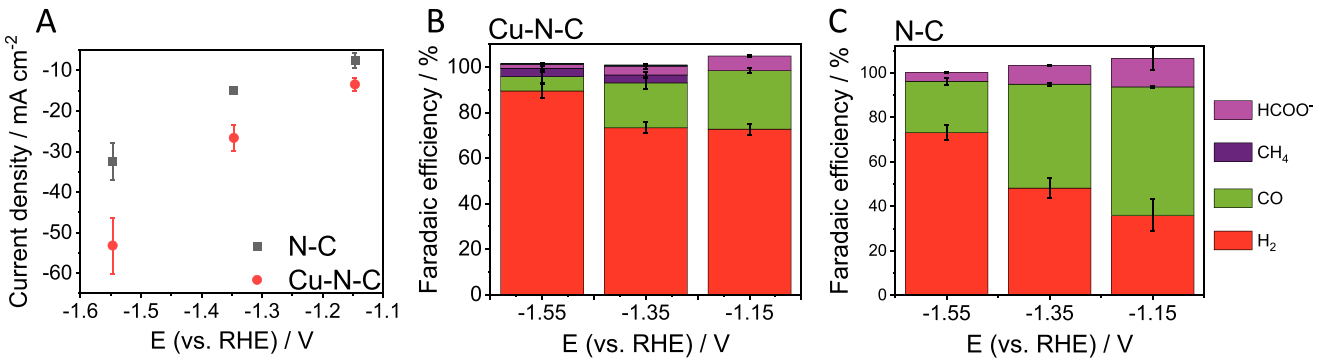

Figure 1. CO_2RR activity and selectivity of Cu-N-C and N-C under potentiostatic conditions in an H-type cell configuration. Measurements were performed in a CO_2-saturated 0.1 M $KHCO_3$ solution. Data points were recorded at the 80th minute of the electrolysis. A) Total current densities. B,C) Faradaic efficiencies for Cu-N-C and N-C (Cu-free support). Error bars represent the standard deviation of measurements performed on at least three separate but identically prepared samples.

absorption spectroscopic (XAS) analysis presented below, confirmed the single-atomic nature of the synthesized Cu-N-C catalyst. We emphasize, however, that under reaction conditions, singly dispersed metal sites are expected to be unstable and tend to aggregate into metal clusters, as recently demonstrated by our group.[24] Additionally, the formation of metallic Zn has also been observed in these types of materials.[39]

The CO_2RR selectivity of Cu-N-C under potentiostatic conditions is presented in **Figure 1**, and compared with that of the Cu-free N-C catalyst. The incorporation of copper dopants led to approximately a 1.5-fold increase in the current density, compared to the Cu-free sample. However, this enhancement in overall activity was primarily attributed to an increased rate of the hydrogen evolution reaction (HER), rather than an improvement in CO_2RR performance. The main product of CO_2RR was CO, accompanied by minor amounts of formate ($HCOO^-$) and methane (CH_4); the latter being detected only on the Cu-containing catalyst. While the Faradaic efficiency for CO on the Cu-N-C catalyst ranged from 6% to 25%, the Cu-free N–C sample exhibited higher CO selectivity, with FE_{CO} values between 23% and 57% within the studied potential window. A similar trend was observed for $HCOO^-$ formation, though with even lower Faradaic efficiencies—4% for Cu–N–C versus 8% for N–C at −1.35 V. Notably, despite the significantly higher total current density measured on Cu-N-C, the CO formation rate (i.e., partial current density) was ≈1.5–2 times lower than on the Cu-free N–C (Figure S8, Supporting Information), clearly indicating that the Cu species in the Cu-N-C sample are primarily selective for HER under potentiostatic conditions. It is important to note that the witnessed differences did not arise from the variations in the electrochemical surface areas, as the double-layer capacitance values of the two catalysts were very close (Figure S9, Supporting Information).

Next, we turned to pulsed conditions (p-CO_2RR). We alternated the potential between a cathodic (more negative) and an anodic (less negative) value. We used 30 s symmetric pulses with equal anodic (t_a) and cathodic times (t_c). A representative pulse profile with the potential and current traces is presented in Figure S10 (Supporting Information). A pulse duration of 30 s was sufficient to ensure that the majority of the current was utilized for faradaic processes rather than double-layer charging (Figure S1 and Note S1, Supporting Information). Furthermore, based on our previous study,[24] which investigated the effect of pulse length on the structure and catalytic selectivity of Cu–N–C, pulsing under these conditions leads to the formation of ultrasmall metallic Cu clusters, accompanied by a reduction in the number of singly dispersed cationic copper sites. This leads to suppressed H_2 formation and enhanced CO_2RR selectivity.

The Faradaic efficiencies under pulsed CO_2RR conditions are presented in **Figure 2**A and Figures S12 and S14 (Supporting Information). Experiments were conducted using three cathodic (−1.15, −1.35, −1.55 V vs RHE) and seven anodic (−0.16, 0.04, 0.24, 0.44, 0.64, and 0.84 V) potential values. Contour plots illustrating the changes in the Faradaic efficiency for the main products, relative to the potentiostatic CO_2 reduction conditions, are shown in Figure 2 B–F. These plots clearly show that pulsing significantly suppressed FE_{H2} when the anodic potential exceeded 0.04 V. The suppression of H_2 formation was most pronounced at intermediate anodic potentials, with the FE_{H2} dropping to as low as 17.5% with the cathodic potential (E_c) of −1.35 V and the anodic potential (E_a) of 0.34 V. This represents a remarkable, roughly 75% decrease as compared to the corresponding potentiostatic condition. Concurrently, both the selectivity and reaction rate for CO_2RR increased significantly under pulsed conditions (see Figure 2A; Figure S14, Supporting Information). Unlike potentiostatic CO_2 reduction, where CO was consistently the dominant CO_2RR product across the potential range, pulsed electrolysis resulted in either CO or methane being the main product, depending on the specific pulse conditions. The product distribution was jointly governed by the values of applied anodic and cathodic potentials. At the least negative cathodic potential (−1.15 V), CO was the primary product, whereas at the most negative potential (−1.55 V), methane became dominant–resembling the known potential dependence of CO_2RR products on metallic Cu electrodes under static conditions.[8,43] Notably, the FE_{CH4} reached up to 50% at E_c = −1.55 V and E_a = 0.34 V pulse potentials. At the intermediate cathodic potential (−1.35 V), however, we observed comparable FE for methane and CO, with the anodic potential determining the favored product. More positive anodic potentials promoted methane formation over CO, reaching nearly 50% FE_{CH4} at E_c = −1.35 V and E_a = 0.84 V, which is a ≈15-fold improvement compared to potentiostatic conditions. These

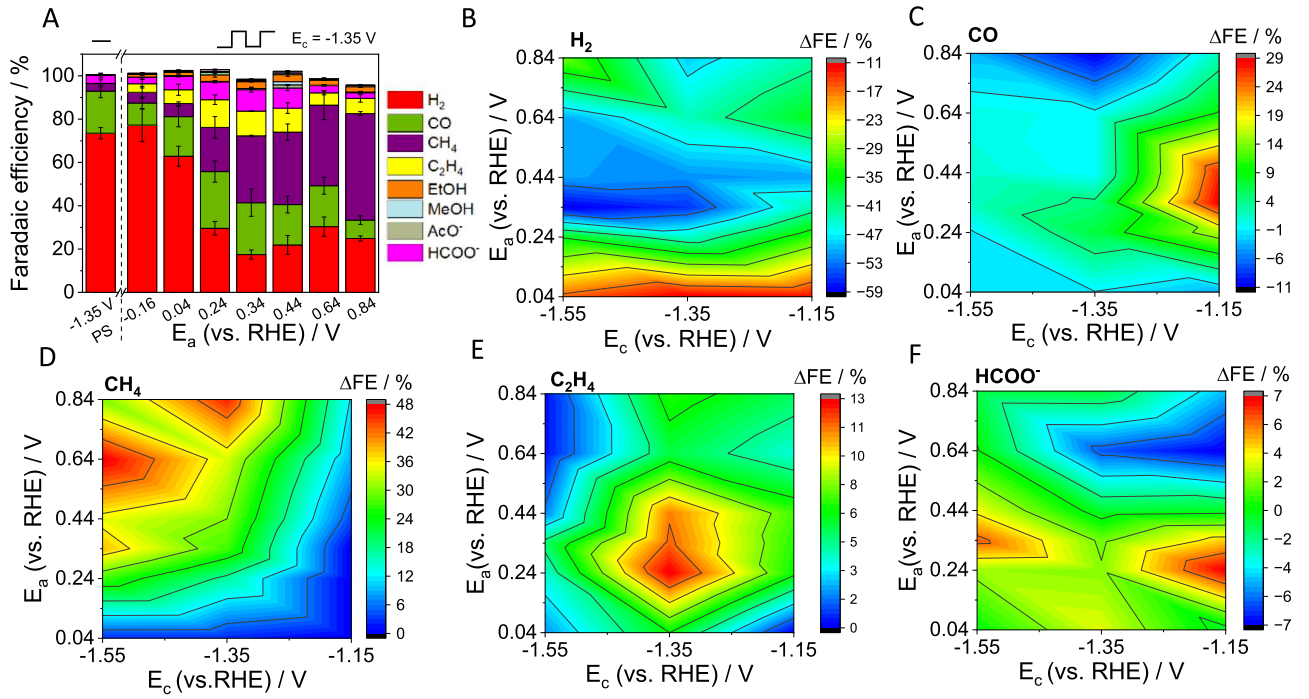

Figure 2. A) Faradaic efficiency of pulsed CO_2RR on Cu-N-C at a fixed cathodic potential (−1.35 V vs RHE) and varying anodic potentials. B–F) Relative change of Faradaic efficiency during pulsed CO_2RR compared to the potentiostatic reduction for the main products as a function of anodic and cathodic potentials. ($\Delta FE = FE_{pulsed} - FE_{potentiostatic}$). Measurements were performed in a CO_2-saturated 0.1 M $KHCO_3$ electrolyte, and products were analyzed after 1.4 h of electrolysis. A rectangular symmetric pulse profile was employed with $t_a = t_c = 30$s. Error bars represent standard deviations of measurements performed on at least two separate samples.

findings suggest that pulsing enhances the binding strength for the CO_{ads} intermediate, facilitating its further reduction to CH_4.

Ethylene formation was also observed on the Cu-N-C catalyst under pulsed conditions, whereas it was not detected under potentiostatic operation. The most favorable conditions for ethylene production were found at intermediate anodic potentials (i.e., between 0.24 and 0.44 V) with a maximum *FE* of 12.8% at $E_c = -1.35$ V and $E_a = 0.24$ V. Among the liquid-phase products (Figure S11, Supporting Information), formate was detected in the highest quantities, with a similar anodic potential dependence as CO, though with approximately three times lower *FE*. Additionally, pulsed conditions enhanced the selectivity toward C_{2+} liquid products, although their cumulative *FE* remained below 8%. Within this group, ethanol showed the highest individual contribution, with a *FE* slightly exceeding 3%.

We also analyzed the partial current densities (*j*) of the major products (Figure S14, Supporting Information), which exhibited trends similar to those observed for the Faradaic efficiencies with respect to anodic potential. The partial current density for H_2 (j_{H2}) decreased during pulsed CO_2RR compared to potentiostatic reduction, while the partial current densities for CO_2RR products increased. This enhancement was particularly pronounced for CH_4 as its partial current density continuously rose with increasing anodic potential, reaching −15 mA cm^{-2} at $E_c = -1.55$ V and $E_a = 0.84$ V—a 7.5-fold increase compared to the potentiostatic reduction. Overall, this analysis demonstrated that pulsed electrolysis enhances not only the Faradaic efficiencies but also the production rates of individual CO_2RR products compared to potentiostatic reduction. Importantly, the observed improvements in the CO_2RR FEs are not solely attributable to suppressed HER. Rather, they reflect a genuine increase in CO_2 RR activity. These findings highlight that, through the careful selection of anodic and cathodic potentials, both the selectivity and current density for a desired product can be effectively tuned using the same Cu–N–C catalyst.

The possible restructuring of the Cu-N-C pre-catalyst samples under both potentiostatic and pulsed CO_2RR conditions was analyzed via high-resolution TEM and energy-dispersive elemental mapping (**Figure 3**; Figures S5–S7, Supporting Information). Notably, no crystalline particles were observed after reaction, except for a few rare Cu nanoparticles detected following 1.4 h of potentiostatic electrolysis at −1.55 V. In contrast, singly dispersed Cu (and Zn) sites remained clearly visible and uniformly distributed within the carbon matrix after reaction for both operating modes.

During the pulsed electrolysis experiments, we observed that the catalytic performance gradually evolved over time. Specifically, the overall reduction current decreased progressively across all applied potential values (Figure S15, Supporting Information), which correlated with a gradual suppression of the hydrogen evolution reaction (HER) (**Figure 4A**). In contrast, the CO_2RR current density remained stable throughout the timeframe of the experiment (1.4 h). In fact, a slight increase in the CO_2RR partial current density was observed during the first ≈30 min of pulsed electrolysis, primarily driven by the rise in the FE_{CH4} over time (Figure 4B). These observations suggest that there are relatively slow structural or chemical changes taking place at the catalyst under pulsed conditions, and mass transport effects (i.e., replenishment of CO_2 at the electrode surface during anodic pulse)

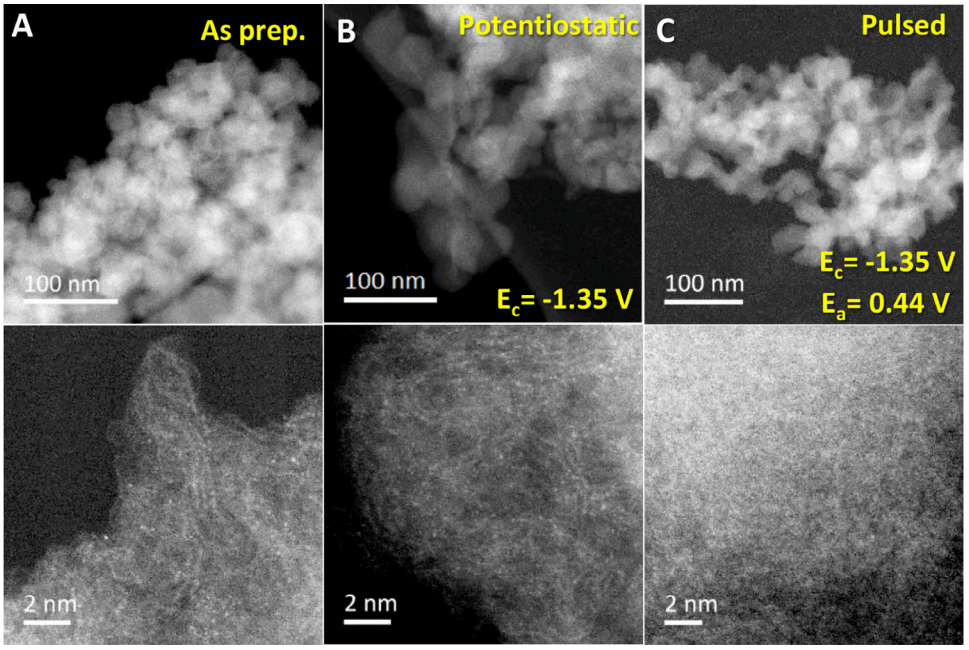

Figure 3. High-angle annular dark field (HAADF) scanning transmission electron microscopy (STEM) images of the copper-nitrogen-doped carbon (Cu-N-C) catalysts before and after CO_2 reduction (CO_2RR). a) As-prepared sample, b) after applying −1.35 V constant potential, c) after pulsed CO_2RR with E_c = −1.35 V and E_a = 0.44 V. Their corresponding high resolution (HR-STEM) images highlight the presence of single atom doping elements.

cannot solely be responsible for the selectivity shift. This assumption is further supported by the observed dependence of the catalytic selectivity on the anodic potential, as well as by the lack of HER suppression at the most negative E_a (−0.16 V) value. Thus, we assume that pulsing induces changes in the interfacial adsorbate coverage (binding energies and surface concentration of reactants and/or intermediates), which happens gradually over the course of hours. Such changes either arise from the dynamic rearrangement of the electric double layer or structural changes in the active sites (e.g., oxidation or hydroxylation, Cu dissolution and subsequent redeposition/redispersion, cluster or nanoparticle formation).

As a control, we evaluated the performance of the Cu-free N–C catalyst in pulsed CO_2RR (Figure S18, Supporting Information). In this case, the product selectivity remained almost unchanged compared to potentiostatic conditions (Figure 1C). Notably, neither methane nor C_{2+} products were detected in the absence of copper, clearly indicating that the effect of pulsing on Cu-N-C is at least in part rooted in the dynamic evolution of the Cu-sites and not solely due to changes in the N-C matrix induced by the pulsing treatment.

To deeper understand the processes happening during the potential pulsing, the reversibility of the process was studied. For this purpose, a CO_2RR sequence was performed consisting of an

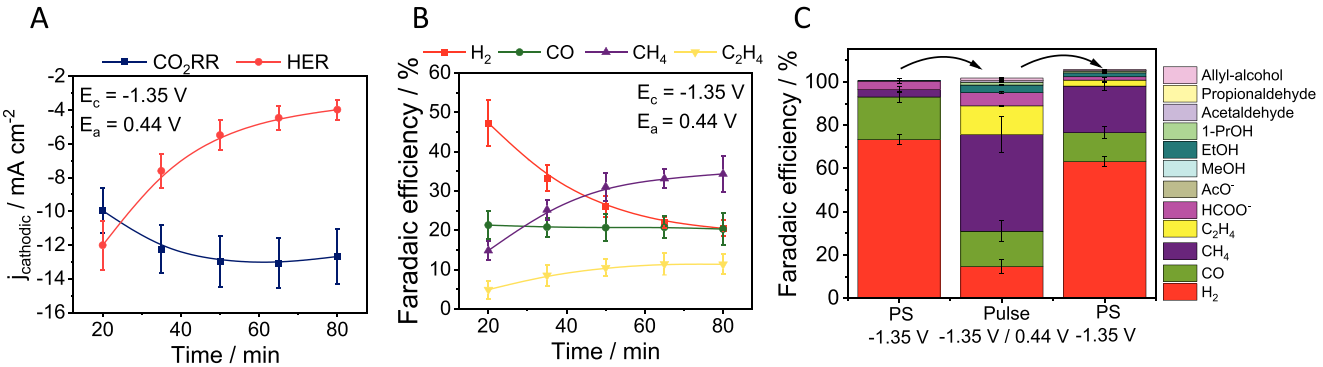

Figure 4. A) Time-evolution of the HER and CO_2RR current densities during p-CO_2RR with E_c = −1.35 V and E_a = 0.44 V. The currents were recorded at the end of the cathodic pulse. B) Time-evolution of the Faradaic efficiencies for H_2, CO, CH_4, and C_2H_4. C) Faradaic efficiencies during a CO_2RR sequence measured on the same catalyst sample. The experiment started with a potentiostatic electrolysis, followed by pulsing (E_c = −1.35 V, E_a = 0.44 V, t_a = t_c = 30 s), then again, a potentiostatic run (2 h each). The cathodic potential was −1.35 V, while the anodic potential was 0.44 V during the p-CO_2RR. Lines serve as a guide for the eye. Error bars represent the standard deviation of measurements performed on at least three individual samples.

initial 2-h potentiostatic reduction at−1.35 V, followed by a 2-h pulsed electrolysis ($E_c = -1.35$ V and $E_a = 0.44$ V), and concluding with another 2-h potentiostatic reduction at −1.35 V (Figure 4C). Notably, the selectivity observed during the second potentiostatic phase differed from that of the initial static reduction on a fresh electrode. Namely, the FE_{H2} remained slightly lower, while the FE_{CH4} increased by a factor of ≈7 relative to the first potentiostatic measurement. Additionally, the total CO_2RR current was also over 15% higher on the pre-pulsed sample (Figure S19, Supporting Information). A similar trend was observed when we performed the same experiment with 0.24 and 0.64 V anodic potentials (Figure S20, Supporting Information). This implies that in addition to reversible changes, pulsed potential CO_2RR also induces irreversible changes in the catalyst structure, which are not fully recovered during a 2-h potentiostatic reduction. As a control, we also run a potentiostatic measurement for the same total duration as the static–pulse–static sequence (6 h). In this case, we observed a slow but steady increase in the FE_{CH4}, accompanied by a slight decrease in the FE_{H2} over time (Figure S21, Supporting Information). However, by the end of the 6-h electrolysis, $FECH_4$ only reached 11%, which is approximately half the value observed at the end of the static–pulse–static protocol. This proves that the increased CH_4-selectivity on the pre-pulsed sample is not merely a consequence of prolonged exposure to the cathodic potential, e.g., to form metallic nanoparticles, but that the periodic perturbation of the catalyst by potential pulses plays a definitive role. The slight variations in the selectivity of the pre-pulsed sample most likely stem from irreversible morphological changes of the electrodes. Indeed, we found that the electrochemical surface area of the Cu–N–C electrodes decreased after both the potentiostatic and the pulsed reduction (Figure S37, Supporting Information). The most notable changes were, however, observed when the anodic potential was between 0.24 and 0.64 V. This is an indication that the most significant morphological changes occur under these conditions, which contribute to the observed selectivity change and the non-complete reversibility of the process.

The relatively slow recovery after pulsing inspired us to increase the t_c/t_a ratio to 300 s/30 s from the above presented 30 s/30 s, therefore leading to practically more relevant conditions by reducing the off-time (from 50% to 9%), where no product formation takes place. In this case, we also observed suppression of HER and an increase in both FE_{CH4} and FE_{C2H4} compared to potentiostatic reduction (Figure S22, Supporting Information). Although the effect of pulsing on CO_2RR selectivity was evident here as well, the Faradaic efficiency for H_2 was slightly higher and that for CH_4 slightly lower after 2 h, compared to the results obtained using symmetric pulses ($t_a = t_c = 30$ s). Moreover, the time required to reach the enhanced selectivity was longer when the t_a/t_c ratio was lower.

2.2. Quasi In Situ XPS

We performed quasi in situ XPS measurements to investigate the chemical changes at the surface of the catalyst after CO_2RR. By using a custom-designed electrochemical cell directly attached to the load-lock chamber of the ultrahigh vacuum system, we were able to perform the sample transfer between the electrochemistry setup and the vacuum chamber, without sample exposure to air. In this way, the possible reoxidation of the catalyst is minimized.

We performed the quasi in situ XPS measurements after performing potentiostatic and *p*-CO_2RR with $E_c = -1.35$ V and varying E_a values, and followed the changes in the N 1s region (**Figure 5**) of the catalyst. In this way, we were able to get insights into the different N defects available on these samples, and their evolution during CO_2RR, which also serve as anchoring defect sites for the Cu single atoms. Before CO_2RR we detected the following distinct N functionalities: Imine N at 397.5 eV, pyridinic N at 398.2 eV, metal-coordinated N (M-N_x) and amine species centered at 399.3 eV, N—H (pyrrolic N + hydrogenated pyridinic N) located at 400.7 eV, graphitic N at 402.0 eV, quaternary N at 403.3 eV and–N-O_x species between 405 and 408 eV.[44–48] After CO_2RR, the intensity of the peaks attributed to oxidized N-species (located above 405 eV) is suppressed, and not only for the potentiostatic but, more surprisingly, for the pulsed reduction too. This means that once these N-species are reduced during the cathodic potential pulse, the periodic application of a more positive potential (i.e., pulsing) does not result in their reoxidation. On the other hand, after CO_2RR, the ratio of the main N broad feature at 400.2 eV increased relative to the one centered at 398.2 eV both for the pulsed and the static conditions. To quantify this change, we fitted the spectra and calculated the ratio of the peak areas for the different N species at higher binding energies (Graphitic N at 402.0 eV + Quaternary N at 403.3 eV + Hydrogenated N at 399.3 eV), to the N-species located at lower binding energies:(Pyridinic N at 398.2 eV + Imine N at 397.5 eV). The former high BE peaks have contributions from the protonated and hydrogenated N-species, while the latter low BE peaks are related to the non-protonated/non-hydrogenated N-moieties[44] (see Figure S4, Supporting Information too). Therefore, a higher ratio in the high BE/low BE components of the N spectrum represents a higher surface H-concentration on the N-doped carbon support. The relative increase in this ratio was significantly lower after pulsed CO_2RR compared to the static reduction (Figure 5D), suggesting that pulsing diminishes surface hydrogenation. Furthermore, when plotting the partial current densities for H_2 versus the relative increase in the high BE/low BE peak ratio after *p-CO₂RR*, we discovered a positive correlation between these two parameters (Figure 5E). This finding indicates that the lower surface H-coverage observed on the carbon support indeed might be related to the suppressed H_2 evolution under pulsed conditions. Nevertheless, this effect alone cannot account for the observed selectivity trends, as a similarly strong suppression of the HER would also be expected on the Cu-free N-C catalyst, which was not the case. Instead, this observation suggests a marked influence of the surface functionalization of the N-doped carbon support on the catalytic behavior of the singly-dispersed Cu active sites.

2.3. Operando X-Ray Spectroscopies

To explain the observed trends in CO_2RR selectivity under static and pulsed conditions, we performed *operando* XAS measurements in QXAFS mode. Our XAS results for the potentiostatic CO_2RR (Figure S24, Supporting Information) are in agreement with our previous reports.[24,39] Specifically, the as-prepared sam-

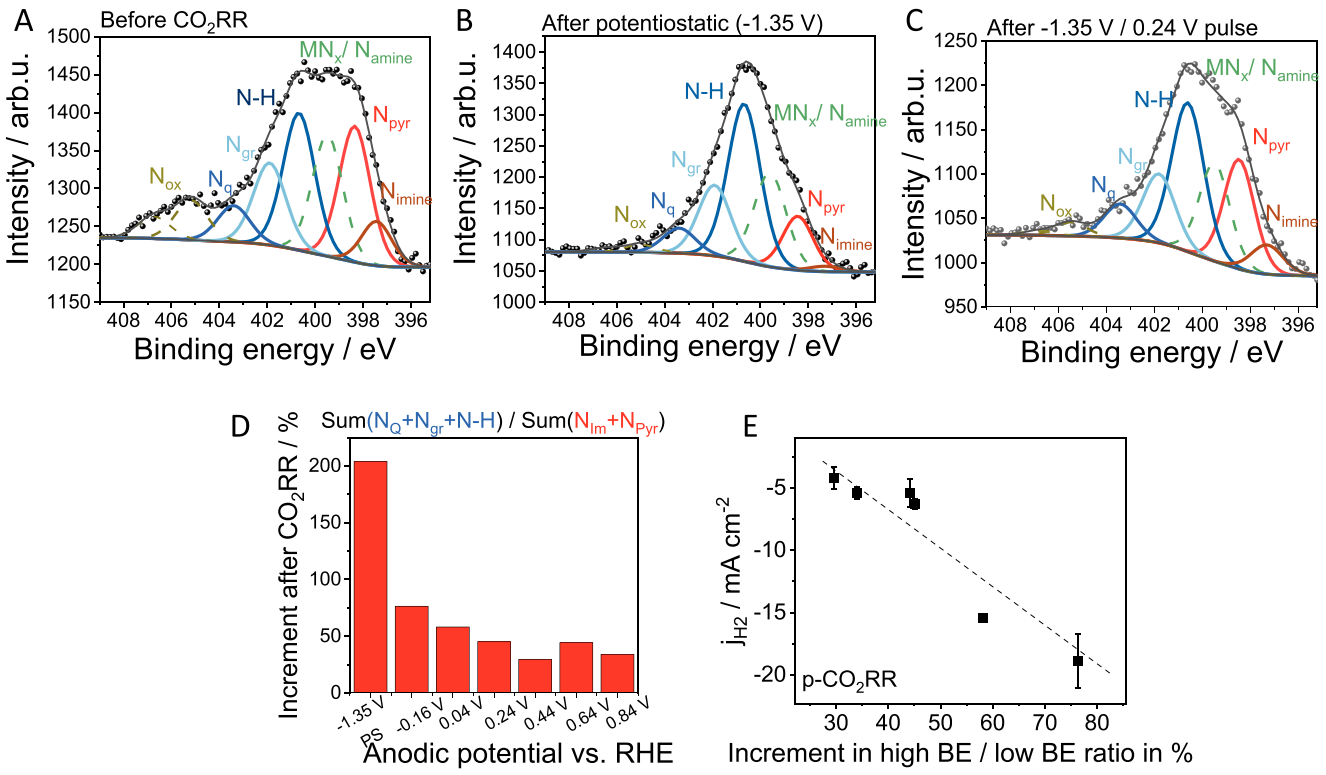

Figure 5. N1s XPS core-level spectra of Cu-N-C catalysts acquired before CO_2RR (A), after potentiostatic CO_2RR (B), and after pulsed CO_2RR (C). In (A), the as-prepared sample was exposed to air before the measurement. The quasi in situ XPS data in B and C were obtained after PS reduction at −1.35 V vs RHE (B) and after p-CO_2RR with E_c = −1.35 V and E_a = 0.24 V vs RHE (C), when the potential was stopped at the anodic value. In B and C, the samples were transferred directly from the electrolysis cell under an Ar atmosphere to the load-lock chamber of the UHV system, to avoid contact with air. The peaks in blue at the higher binding energy represent the protonated/hydrogenated N-species, while the ones colored in red are the dehydrogenated N-moieties. D) Increment in the ratio of the high BE/low BE components after CO_2RR with E_c = −1.35 V and different E_a values. E) Correlation between the H_2 partial current density in p-CO_2RR and the increment in high BE/low BE components after p-CO_2RR.For the experiments, a 0.1 M $KHCO_3$ electrolyte was used, and the CO_2RR was performed for 1.4 h.

ples feature singly dispersed Cu^{2+} species that predominantly convert into metallic clusters under constant cathodic potential. The transformation is reversible: after lifting the cathodic potential, the aggregated metallic Cu species redisperse back into cationic species that are spectroscopically very similar to the original Cu species in the as-prepared Cu-N-C catalysts. To further support our conclusion on the reversible formation and redispersion of metallic clusters, we carried out *operando* vtc-XES and HERFD-XAFS measurements (**Figure 6**). These advanced techniques provide better sensitivity to the presence of different ligands around the central Cu species, and can help to resolve different Cu species with low spectroscopic contrast.[49,50] In particular, the vtc-XES technique is attractive due to its ability to discriminate between neighboring atoms with similar photoelectron scattering properties, facilitating the identification of active structural motifs.[51–53]

In our case, we observe that the HERFD-XANES and the vtc-XES spectra collected before and after reaction resemble those for octahedrally coordinated Cu^{2+} species. Nonetheless, they are distinct from the spectra of standard Cu reference materials. We attribute this difference to the formation of in-plane Cu—N bonds with the support, coexisting with axial Cu—O bonds.[24,39] At the same time, the spectra collected during CO_2RR strongly resemble the corresponding spectra for metallic Cu, suggesting that the majority of Cu species is converted into metallic particles. The suppressed amplitude of post-edge oscillations in the operando HERFD-XAS spectrum with respect to those in the metallic Cu reference could be attributed to the very small sizes of the formed Cu particles.[54] Taking together, our XAS, HERFD-XAS, and vtc-XES data strongly support our model where singly dispersed Cu species under cathodic potential are converted into metallic Cu clusters. The latter, in turn, are redispersed after lifting the cathodic potential and/or applying an anodic potential. Importantly, the redispersion does not involve the formation of new copper oxide or hydroxide species. Instead, the metallic clusters return to a state which is spectroscopically indistinguishable from the original one, thus attributed to singly dispersed Cu^{2+} cations anchored to N dopants in the carbon support.

Under pulsed reaction conditions, periodic switching between cationic Cu and metallic Cu clusters is clearly visible in QXAFS data (**Figure 7**). We can quantify these transformations by using linear combination analysis of XANES spectra to estimate the fractions of metallic and cationic Cu species (Note S2, Supporting Information), and principal component analysis (Note S3 and Figure S32, Supporting Information) to rule out the presence of additional Cu species.[24] EXAFS data fitting is applied to extract information about average coordination numbers (Figure S26 and Table S3, Supporting Information), hence, about the av-

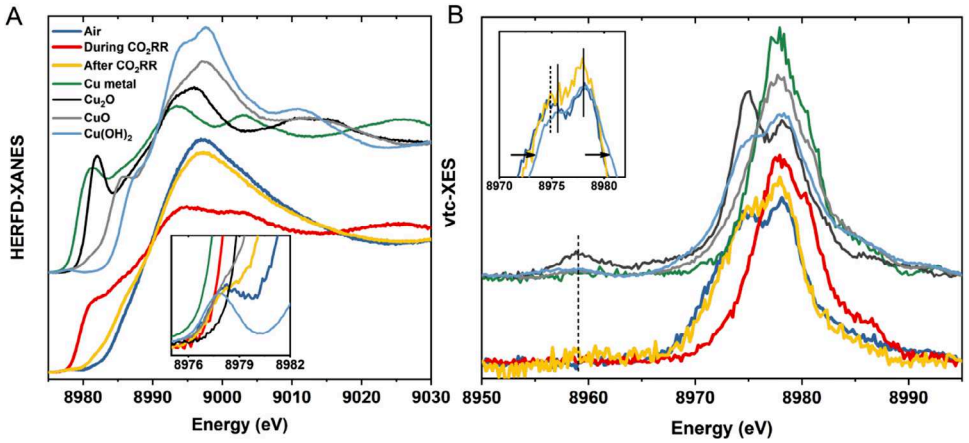

Figure 6. Cu K-edge HERFD-XANES (a) and vtc-XES (b) data collected for the as-prepared Cu-N-C catalyst and the same catalyst under potentiostatic CO_2RR at −1.35 V in a 0.1 M $KHCO_3$ electrolyte, as well as after CO_2RR in air. Spectra collected during and after reaction conditions are collected at least 1 h after the onset of CO_2RR. Reference spectra for Cu foil, Cu_2O, CuO, and $Cu(OH)_2$ are also shown.

erage sizes of the Cu clusters formed (Figure S27, Supporting Information). Such an analysis suggests that under static reaction conditions (at −1.35 V_{RHE}), particles with a size of ≈1.5 nm are formed (Note S4, Supporting Information). Under pulsed reaction conditions, in turn, we observe periodic changes in the concentrations of metallic Cu species as well as in the average Cu—Cu coordination numbers (Figures 7 and 8). The average values of these quantities and magnitudes of their oscillations depend strongly on the values of the applied pulse potentials.

Representative LCA-XANES fits of the QXAFS data collected under pulsed conditions are shown in Figure S29 (Supporting Information), while the obtained time-dependent changes in the fractions of singly dispersed Cu sites are shown in Figure 7b–d and, in more detail, in **Figures** S8 and S34 (Supporting Information). Results for pulse sequences with E_a values of −0.16, 0.44, and 0.84 V are shown here, while the results for pulse sequences with E_a values of 0.04, 0.24, and 0.64 V are shown in Figures S30 and S31 (Supporting Information). Representative fits of the EXAFS spectra collected under the pulsed CO_2RR are shown in Figure S33 (Supporting Information). Figure 8 shows the time-dependent evolution of the structure parameters and concentrations of different Cu species (Note S4, Supporting Information) as extracted from EXAFS fits.

From these data, one can see clear differences in the evolution of the Cu sites under pulsed CO_2RR with different E_a values. The sustained, pronounced switching between states containing mostly metallic species during the cathodic potential pulse, and mostly singly dispersed species during the anodic potential pulse

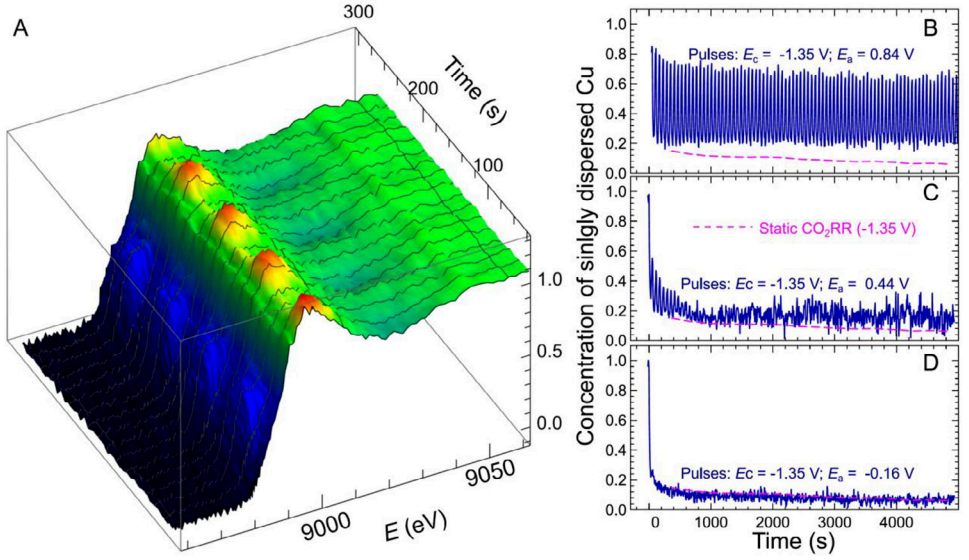

Figure 7. a) Cu K-edge XANES for the Cu-N-C catalyst under pulsed CO_2RR with E_c = −1.35 V and E_a = 0.84 V. b–d) results of LCA-XANES for the Cu-N-C catalyst under pulsed CO_2RR with identical E_c = −1.35 V and varying E_a = 0.84 V (b), 0.44 V (c) −0.16 V (d). Evolution of the concentration of singly-dispersed Cu sites is shown. The LCA-XANES results obtained for Cu-N-C catalyst under static CO_2RR are also shown as a dashed magenta line in (b–d).

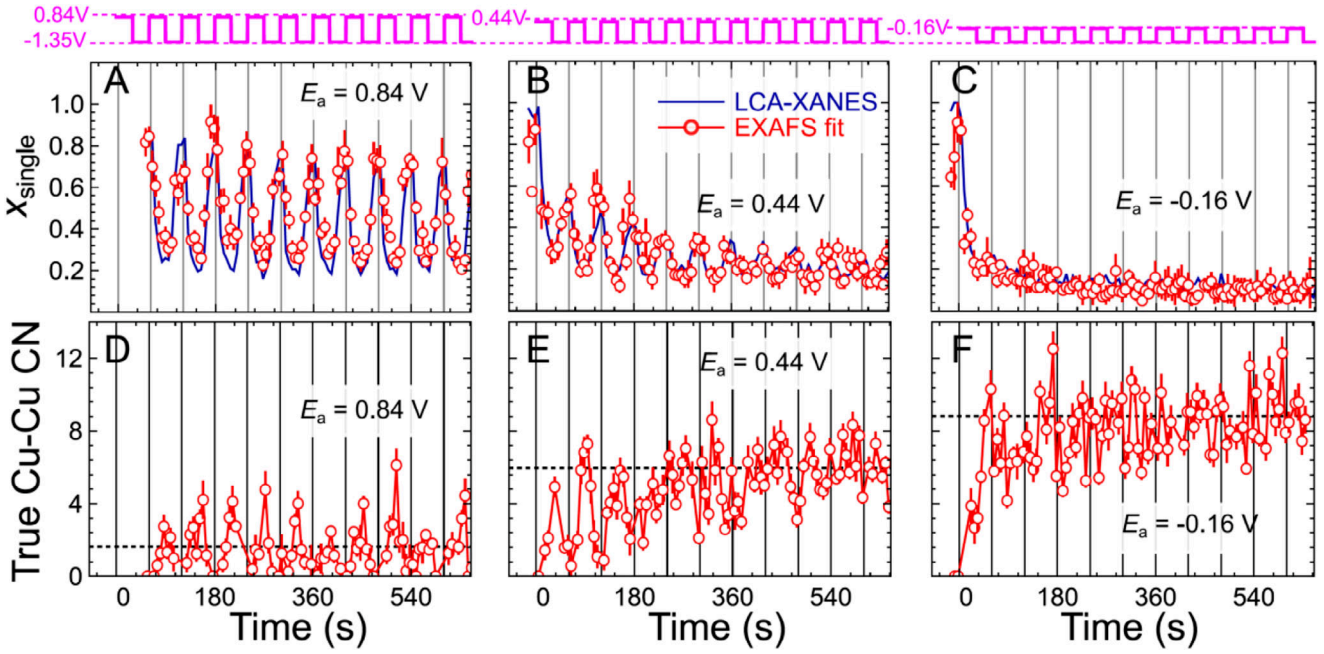

Figure 8. Results of LCA-XANES and EXAFS data fitting for Cu-N-C catalyst under pulsed CO_2RR with $E_c = -1.35$ V and $E_a = 0.84$ V (a,d), 0.44 V (b,e), and −0.16 V (c,f). (a–c) show the fraction of singly dispersed Cu species, as independently obtained from LCA-XANES and EXAFS-derived Cu-X coordination numbers. d–f) show the true Cu–Cu coordination number (corrected for the presence of different Cu species) $\tilde{N}_{Cu-Cu} = N_{Cu-Cu}/(1 - x_{single})$. Black dashed lines in (d–f) mark the average true Cu–Cu coordination number at the end of the first 600 s under pulsed CO_2RR.

takes place only at the higher E_a values (0.64–0.84 V). Under such potential pulses, the average concentration of singly dispersed Cu sites is much higher than under potentiostatic CO_2RR conditions with the same negative applied potential ($x_{SAC} = 0.67$ under pulses with $E_c = -1.35$ V and $E_a = 0.84$ V vs 0.06 at static conditions at $E_c = -1.35$ V). Importantly, even during the cathodic pulse, the concentration of the single Cu sites is about three times larger than under the static CO_2RR conditions. At lower E_a values (0.24–0.44 V), in turn, already after the first few potential pulses, the sample is dominated by metallic Cu. The redispersion of Cu sites under the anodic potential pulse has a continuously decreasing magnitude, and is not visible anymore in our XAS data after 600 s. We attribute it to the fact that the redispersion of clusters is slow at these anodic potentials. After the first 600 s, the composition of the catalyst remains stable for at least 6 h, as demonstrated in our extended duration XAS measurements (Figure S31, Supporting Information), hence the observed catalytic performance decrease shown in Figure S23 (Supporting Information) is not related to leaching or structural changes of the Cu sites. We propose that the observed performance deterioration is more likely due to degradation of the N-doped carbon support, either through carbon corrosion (oxidation) or loss of hydrophobicity, which ultimately shifts the selectivity toward hydrogen evolution.

For even lower E_a values (from −0.16 to +0.04 V), the catalyst is in a predominantly metallic state already after the first two cathodic pulses, and further evolution of the catalyst resembles strongly that under potentiostatic CO_2RR. Useful clues for explaining such different behavior of our catalyst can be gained from examining our EXAFS fitting results for the Cu—Cu bond contribution (Figure 8d–f). As expected, the true Cu–Cu coordination number after the first potential pulse is similar for all E_a values and is ≈4 in all cases. From Figure S27 (Supporting Information), we can estimate that this corresponds to very small Cu particles with ≈0.5 nm in size, namely, particles containing less than 13 Cu atoms. If the E_a values are sufficiently large, these small particles are completely redispersed during the anodic pulse, and the process is repeated from scratch during the next pulse cycle. The Cu–Cu coordination number thus oscillates between 0 and ≈4 in this case. For lower E_a values, however, the Cu clusters are not completely destroyed during the anodic pulse. As a result, during the next pulse cycle, the surviving Cu clusters can get increasingly larger. For the lowest E_a values (e.g., E_a =−0.16 V), the redispersion of the Cu clusters hardly takes place, and the final Cu–Cu coordination number is ≈8.8, which corresponds to a particle size of ≈1.4 nm, and is just slightly smaller than that obtained under stationary CO_2RR conditions (Figure S27, Supporting Information). For intermediate E_a values, in turn, the distribution of particle sizes is non-unimodal. Indeed, here the larger Cu nanoparticles (with sizes similar to those observed under stationary CO_2RR) that are not redispersed from the previous cycles coexist with ultrasmall Cu clusters regenerated at each potential cycle.[24] We also note that in all cases the metallic Cu clusters coexist with remaining singly dispersed cationic Cu sites, and even at the lowest E_a values ≈10% of the Cu remains within these cationic Cu species (Figure S34b, Supporting Information).

In contrast to the pronounced effect of the E_a value on the structure of the catalyst, the value of the cathodic potential E_c seems to affect less drastically the formation of metallic clusters, at least in the potential range investigated and for the fixed pulse durations (30 s) that we have chosen here. Indeed, already under potentiostatic CO_2RR conditions, we observe that

the evolution of the catalyst under −1.15, −1.35, and −1.55 V is similar (Figure S35a, Supporting Information). This also agrees with the conclusions of our previous work, where no strong changes in the Cu–N–C catalyst evolution were observed under different applied static potentials.[39] When exposed to pulsed CO_2RR conditions with different E_c values (Figure S35b–e, Supporting Information), the changes in the catalyst structure induced by potential pulses seem to be similar, as long as the E_a value is kept the same. The selectivity shift from CO to methane, thus in this case, is potential, rather than structure dependent, and is associated with the change in the CO_{ads} intermediate binding strength altered by the cathodic potential, similarly as for the potentiostatic reduction. Clearly, at even less negative E_c values (i.e., > −1.1 V_{RHE}), a larger effect of E_c on the catalyst structure could be expected. However, these lower values of the working potential are less relevant for CO_2RR on Cu–N–C.

We note that under all pulsed conditions, the Cu fluorescence signal, which is related to the concentration of Cu species in our samples, decreases in intensity during pulsing (Figure S28, Supporting Information). This loss takes place during the first 15 min but in almost all cases accounts for less than 30% after 1.4 h of pulsed CO_2RR. Lack of further changes in the catalyst loading, once the stationary state is reached, even in the presence of strong periodic oscillations between the cationic and metallic catalyst state, strongly suggests that the dissolution of metallic Cu plays no significant role in the redispersion mechanism of Cu clusters. Instead, it is likely to be driven by strong particle interactions with the N-C support.[41]

To check for the presence of other irreversible changes in the catalyst structure (besides loss of catalyst), we performed measurements under static CO_2RR conditions (−1.35 V_{RHE}) for a sample that was first exposed to pulsed CO_2RR ($E_c = -1.35\ V_{RHE}$, $E_a = 0.44\ V_{RHE}$) for 83 min (Figure S36, Supporting Information). After 1 h of static CO_2RR, the obtained XAS spectra are practically indistinguishable from those collected after 1 h of static CO_2RR over a fresh sample. This strongly suggests that the aforementioned irreversible changes in the catalytic selectivity (Figure 4C) are indeed linked to the changes in the N–C support itself, rather than in the Cu local structure or chemical state.

2.4. Discussion

Based on the quasi in situ XPS and operando X-ray spectroscopy results, we conclude that the Cu–N–C system under investigation is inherently complex, with multiple catalytic sites coexisting and dynamically evolving during reaction. The observed selectivity changes thus cannot be solely attributed to a single factor, but multiple processes must be considered. We propose the following mechanisms to explain the observed catalytic activity/selectivity change during pulsed CO_2RR on the Cu-N-C catalysts. (i) Pulsing contributes to CO_2 replenishment.[55] (ii) Pulsing the potential reduces the extent of surface hydrogenation on the N–C support as suggested by XPS analysis. This diminished surface H-coverage under pulsed conditions—compared to the potentiostatic reduction—leads to a suppression of the hydrogen evolution reaction (HER). We further propose that this decrease in H_{ads} coverage is accompanied by an increase in the surface concentration of adsorbed CO_{ads}. This altered surface functionality of the N–C support strongly influences the catalytic activity of the Cu sites. This, in turn, enhances the rate of methane formation and enables the onset of ethylene production even at the lowest anodic potential studied (E_a = −0.16 V), when the average Cu–Cu coordination number (and, thus also the particle size) is very similar to that under the potentiostatic conditions. (iii) Pulsing also alters the chemical state and structure of the Cu active sites. The highest CO_2 RR selectivity was observed within the anodic potential range of 0.24–0.44 V. In addition to the more favorable surface functionality of the N–C support in this anodic potential range, the Cu sites are also greatly affected in this regime. These species are unambiguously responsible for the formation of hydrocarbon and C_{2+} oxygenate products, since they were not detected in the absence of copper (bare N–C catalyst) either under potentiostatic or under pulsed electrolysis conditions.

Operando XAS, HERFD-XAS, and VtC-XES data indicate that two distinct Cu species coexist in the Cu–N–C catalyst under both static and pulsed CO_2 RR conditions: i) metallic Cu nanoparticles or clusters of varying sizes, and ii) singly dispersed Cu sites. Both of these species contribute to the overall catalytic functionality, but they exhibit clearly distinct selectivities. Two factors distinguish the structure of the catalyst under pulsed CO_2RR conditions from that under static CO_2RR conditions: i) a larger fraction of singly dispersed Cu sites, and ii) the smaller sizes of the metallic Cu clusters. Increasing the anodic potential amplifies both these structural differences, as illustrated in **Figure 9**.

At lower E_a values (−0.16 V), both the fraction of metallic Cu clusters and their sizes are very similar to those under static CO_2RR. Consequently, the catalytic selectivity is also largely similar. However, a slight enhancement in methane formation and the emergence of ethylene can already be observed. We attribute these changes to support effects and improved reactant replenishment induced by the pulsing conditions. At higher E_a values (0.24–0.44 V), in contrast, the average coordination number of metallic copper gradually decreases, while the fraction of singly dispersed cationic copper increases. As found in our previous work,[24] where we investigated the effect of pulse durations on Cu-N-C selectivity, larger Cu clusters favor CO and ethylene formation, while on ultrasmall clusters, methane is the preferred product. This parallels our present findings, where the decrease in particle size is induced by applying a higher anodic potential rather than shorter cathodic pulse durations. In both cases, when the Cu–Cu coordination number is lower, the FE of methane increases, at the expense of CO and ethylene. The fact that very similar selectivity trends are observed in these two studies underscores the universal and critical role of the Cu–Cu coordination number (or cluster/particle size) as a descriptor for Cu-N-C selectivity trends, regardless of the exact mechanism of how the decrease in Cu–Cu coordination number is achieved. Indeed, experimental evidence and DFT simulations in a recent work[56] suggest that undercoordinated Cu sites in ultrasmall Cu clusters may favor the CO_2 conversion to methane due to a lower reaction energy for the hydrogenation of CO_{ads}. On the other hand, we note here that previous reports in the literature suggested that very small Cu particles favor HER over CO_2RR, and that the main CO_2RR product for such particles is expected to be CO.[57,58] Nonetheless, these previous reports concern particles that are at least a few nanometers in size. Our present study

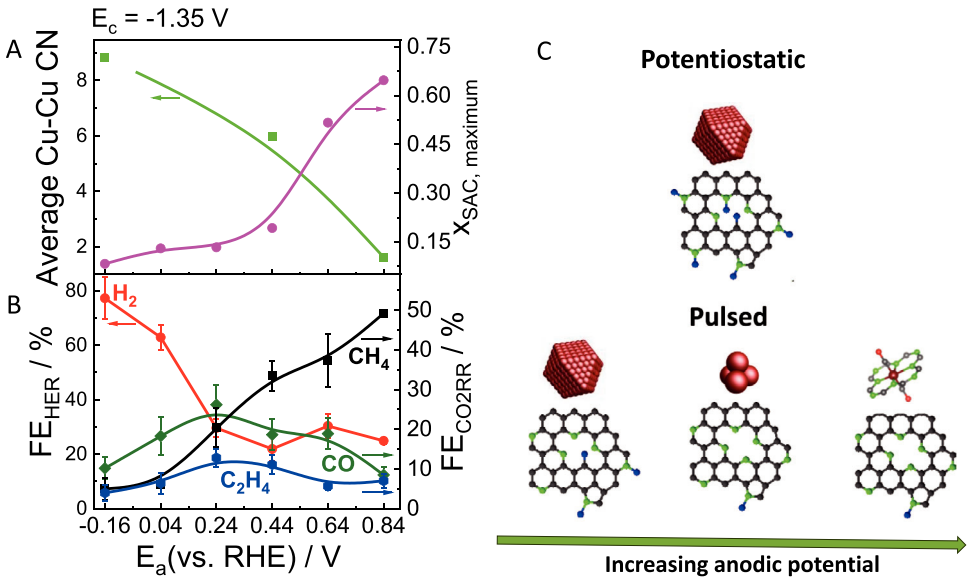

Figure 9. A) Correlation between the average Cu coordination number, the fraction of singly dispersed Cu species, and the catalytic selectivity. B) Schematic summarizing the changes in the catalyst structure with the applied anodic potential. The N-C support and the Cu species are separated for better visibility.

allows us to probe the CO_2RR functionality of particles that are of subnanometer size, which may more strongly affect their catalytic properties.[37,59]

Besides the formation of ultrasmall Cu clusters, a possible smaller local pH at high anodic potentials (>0.44 V) may also contribute to the increase in CH_4 and decrease in C_2H_4 selectivity, as well as to the slight increment of HER, as suggested for metallic Cu-electrodes previously.[26] In this case, the higher H^+ concentration in the electrolyte close to the electrode surface will favor protonation of CO_{ads} instead of C—C coupling. Finally, the slight increase of HER observed at these highest anodic potentials could also be related to the increased amount of singly dispersed Cu sites, which favor HER versus CO_2RR.

In prior reports, high selectivity for C_{2+} products on Cu single atomic pre-catalysts during static CO_2RR was also reported and attributed to the formation of Cu clusters under reaction conditions.[32,38] In our present work, even though Cu clusters were present during static reduction with significantly larger size (≈1.5 nm) than under pulsed conditions (≈0.7 nm at E_a = 0.44 V), ethylene was only formed when HER was suppressed by pulsing. This observation strongly suggests that, beyond the size of the operando formed Cu clusters, the morphology and surface chemistry of the carbon support also play a major role. Furthermore, we assume that although the presence of Cu clusters is a prerequisite for efficient C—C coupling, the remaining Cu single-sites in their vicinity may also play a role. This could also explain the large discrepancy in the literature regarding the CO_2RR selectivity of Cu-N-C catalysts.

Finally, we comment on the time-dependency of the catalytic properties and their correlation to the evolution of the catalyst structure. As can be seen from Figure 6, during the prolonged exposure to pulsed conditions, the fraction of metallic Cu sites increases. Major changes happen during the first 600 s of electrolysis. Nonetheless, the product selectivity changes over a significantly longer time scale (i.e., 1.4 h). Unfortunately, our experimental setup with gas chromatography used for the product analysis did not allow us to reliably analyze the FE of the products at the beginning of the electrolysis (large headspace volume, thus long equilibration time needed). Nonetheless, the Cu-content and the chemical state of the Cu sites appear to be already stabilized when we still observe significant selectivity changes. This suggests that slow chemical/physical changes in the N-doped carbon structure might also take place, for instance, gradual suppression of the surface hydrogen content which may be responsible for this time-dependent selectivity, instead of changes related to the Cu sites. The continuous decrease of the selectivity toward CO_2RR products after 1.4 h can be presumably related to the loss of hydrophobicity of the carbon-based catalyst and the carbon paper support by electrowetting.

3. Conclusion

In summary, we found that pulsing the potential is an effective way to tune the CO_2RR selectivity of a Cu-N-C catalyst. While under potentiostatic conditions, the catalyst produced mainly hydrogen, a remarkable enhancement in the CO_2RR selectivity was achieved under pulsed conditions. The product distribution largely varied with the applied anodic potential, as methane dominated at the largest positive anodic values, meanwhile lower anodic potentials favored CO and C_{2+} product formation. Although the interplay of several processes contributes to the observed selectivity trends, two main factors were identified by using quasi in situ XPS and *operando* X-ray spectroscopies. On one hand, pulsing alters the surface functionality of the N-doped carbon support, resulting in the suppression of the parasitic HER. On the other hand, the fraction and size of the metallic Cu-clusters formed during operation also vary, which depends on the applied anodic potential. This determines the competition between C_1 and C_{2+} products. Here, we demonstrated that by changing the potential values of the p-CO_2RR, the size of the copper clusters

and fraction of singly dispersed Cu sites can be similarly tuned as was reported for the pulse lengths recently. As pulsing can lead to special reaction environments and catalytic functionalities, which cannot be achieved under static conditions, pulsed CO_2RR on metal-nitrogen-doped carbons will not only lead to unique product selectivities but will also largely contribute to our mechanistic understanding of CO_2RR on this catalyst family. Moreover, reversible cluster formation from single metal sites is not unique for Cu, but could take place on other metal centers too,[39] thus p-CO_2RR may also be successfully applied to M-N-C catalysts with different metal sites in the future as well.

4. Experimental Section

Catalyst Synthesis: First, a zeolitic imidazolate framework (ZIF-8) was synthesized starting from 2-methylimidazole and zinc nitrate. In a typical synthesis, 4.24 g $Zn(NO_3)_2{\cdot}6\,H_2O$ and 4.92 g 2-methylimidazole were dissolved in 500 mL methanol, heated to 60 °C, and stirred for 24 h under reflux. The obtained ZIF-8 powder was collected by centrifugation, washed thoroughly with methanol (2x) and ethanol (1x), and dried at 60 °C in air. Then, it was pyrolyzed in a tube furnace in Ar flow (100 mL min^{-1}) at 1000 °C for 1 h. The heating rate was 5 °C min^{-1}. At 1000 °C, most of the coordinated Zn was reduced to metallic Zn, which evaporated at this temperature (boiling point of Zn is 907 °C), leaving behind a porous N-doped carbon structure. The obtained N-C was subjected to acid washing for 24 h, using an excess amount of 20 wt.% HNO_3 at room temperature, to remove remaining crystalline Zn-phases. Finally, the samples were washed thoroughly with ultrapure water until a close to neutral pH was reached.

To synthesize the Cu-N-C catalysts, 200 mg N-C was dispersed in a solution (20 mL) containing 6 mM $Cu(NO_3)_2\ 3\ H_2O$ in isopropanol. The suspension was sonicated for 2 h (≈40 °C), then stirred at room temperature for another 2 h. The Cu^{2+}-impregnated N-C (Cu-N-C precursor) was collected by centrifugation, dried at 60 °C in air, and heat-treated in Ar flow (100 mL min^{-1}) at 700 °C for 1 h. Finally, the obtained Cu-N-C was stirred in 20 wt.% HNO_3 for 24 h at room temperature, and was washed thoroughly with ultrapure water until a close to neutral pH was reached. The final catalyst was dried in air at 60 °C. The Cu-free N-C sample was synthesized the same way, except for bypassing the impregnation step and the second acid-washing, which resulted in an increased residual Zn content.

Electrode Preparation: For the electrochemical measurements, the catalysts were spray-coated onto a pre-heated (≈90 °C) carbon paper (Freudenberg H15C13). The catalyst ink contained 40 mg (Cu-)N-C catalyst, 100 µl Nafion 117 solutions (5%, Sigma–Aldrich), 3.2 mL isopropanol, and 3.2 mL ultrapure water. The mass loading of the electrodes was 0.5 ± 0.05 mg $cm^{-2,}$ and the geometric surface area was ≈0.5 cm^{-2} (the exact value was always measured for each sample).

Electrochemistry Measurements and Product Detection: The electrochemical measurements were performed using an Autolab PGSTAT302N potentiostat/galvanostat. The working electrode was the catalyst-coated carbon paper with ≈0.5 cm^2 geometric surface area. The counter electrode was a platinum mesh. Potentials were measured against a leak-free Ag/AgCl electrode, having a 0.242 V potential versus the standard hydrogen electrode. Potentials are, however, reported throughout the text versus the reversible hydrogen electrode (RHE), calculated using the following equation: E (vs RHE) = E(vs Ag/AgCl) + 0.242 + 0.059·pH. No IR-correction was performed.

CO_2 reduction experiments were performed in a gas-tight two-compartment H-type cell. The cathode and anode compartments were separated by a Selemion anion exchange membrane to avoid product mixing. The electrolysis was performed in a 0.1 M $KHCO_3$ solution pretreated with an ion-exchange resin (Chelex 100 Resin sodium form; Bio-Rad) to remove incidental metal contaminants.CO_2 was continuously bubbled through the anolyte and catholyte with a 20 mL min^{-1} flow rate. The gas outlet of the cathode compartment was directly connected to the injector port of the gas chromatograph via a 6-port valve, allowing online detection of the gaseous products. Samples were automatically injected in 15-minute intervals during the reaction.

Gas products were detected and quantified by an Agilent 7890B gas chromatograph. The products were separated by different columns (Molecular sieve 13X, HayeSep Q, and Carboxen-1010 PLOT) and subsequently quantified with a flame ionization detector (FID), as well as a thermal conductivity detector (TCD).

In the liquid phase, acetate and formate concentrations were analyzed by high-performance liquid chromatography (HPLC, Shimadzu prominence) equipped with a NUCLEOGEL SUGAR 810 column and a refractive index detector (RID). Other liquid products (alcohols and aldehydes) were quantified with a liquid GC (L-GC, Shimadzu 2010 plus) equipped with a fused silica capillary column and FID detectors.

Faradaic-Efficiency Calculation: The Faradaic efficiencies (FE) of the gas products were calculated using the following equations:

$$I_{i,partial} = V \cdot f \cdot \frac{n_i \cdot F \cdot p_0}{RT_0} \cdot \frac{t_a \cdot t_c}{t_c} \quad (1)$$

$$FE\ (\%) = \frac{I_{partial}}{I_{total}} \cdot 100\% \quad (2)$$

V: volume concentration of gas productsobtained from the GC measurements; *f*: volumetric flow-rate of the gas stream leaving the cathode compartment of the cell measured by an universal flow meter (ADM 100, Agilent Technologies); n_i: number of transferred electrons for a certain product; I_{total}: total current density measured during electrolysis at the time of injection into the gas chromatograph; $I_{partial}$: partial current density of a certain product; F: Faraday constant (96485 C mol^{-1}); R: universal gas constant (8.314 J mol^{-1} K^{-1}); T_0: temperature (273.15 K); p_0: pressure (101 325 Pa); t_a: anodic time (time spent at the more positive potential during pulses); t_c: cathodic potential (time spent at the more negative potential during pulses).

In case of the potentiostatic measurements $t_a = 0$ and $t_c = 1$. During the pulsed CO_2RR, I_{total} was read at the end of a cathodic pulse.

The Faradaic efficiencies of the liquid products were detected at the end of the electrolysis, i.e., after accumulation throughout the measurement time.

$$FE_{i,liq}\ (\%) = \frac{c_i * V_{el} * F * n_i}{Q_{total}} \cdot 100\% \quad (3)$$

V_{el}: volume of the electrolyte, Q_{total}: total charge passed throughout the electrolysis.

During *p*-CO_2RR Q_{total} was determined by integrating the *I*–*t* curves over the total reaction time during the cathodic pulses. The cathodic current was estimated to be the current at the end of each cathodic pulse.

$$Q_{total,p} = \sum_i I_{c,i} * t_{c,i} \quad (4)$$

As the capacitive charge at the beginning of an anodic and cathodic pulse closely balances each other, the mathematical integration of the whole current profile ($Q_{total} = Q_{cathodic} - Q_{anodic}$) is equivalent to the reduction current used for the CO_2 conversion. Even though the anodic current does not decay to zero during the anodic pulse, this unbalanced anodic charge (related to the oxidation of the catalyst itself or eventually reaction products or intermediates) is negligible compared to the cathodic charge. Thus, this imposes only minor uncertainty in calculating the cathodic charge, therefore, in the Faradaic efficiency of liquid products.

Electron Microscopy (EM): Images were acquired using a probe-corrected JEM-ARM 200F (JEOL, Japan) scanning transmission electron microscope (STEM) equipped with a cold field emission gun (CFEG) operated at 200 kV. The high-angle annular darkfield (HAADF), annular brightfield (ABF), and brightfield (BF) detector signals were collected from an electron probe with a 14.2 mrad convergence semi-angle and a 90–370, 12–40, 18 mrad collection semi-angle, respectively. The beam current was

kept at 11 pA, and its resulting electron dose was scaled by the pixel size. Image acquisition and manipulation were performed with DigitalMicrograph software v2.4 (Gatan, USA).

Energy-dispersive X-ray Spectroscopy (EDS) spectra and elemental mapping were acquired using a Talos F200X (ThermoFisher Scientific, USA) STEM operated at 200 kV and equipped with four silicon drift detectors (SDDs). The 72 pA electron beam with a 10.5 mrad probe convergence semi-angle was scanned across the region of interest under a continuous frame acquisition mode. The EDS quantification was performed using Velox software v1.4.2 (ThermoFisher Scientific, USA). To reduce the background signal of the carbon framework, the net (baseline intensity counts removed) elemental maps are displayed to highlight the presence of the doping heavy metals.

X-Ray Photoelectron Spectroscopy (XPS): XPS spectra were acquired on a SPECS spectrometer with an Al Kα source (300 W, 12.52 kV). Survey spectra were acquired with 100 eV pass energy, 0.1 s dwell time, 0.75 eV step size, and 2 scans. The N 1s and the metal 2p regions were recorded with 30 eV pass energy, 0.3 s dwell time, 0.15 eV step size using 20 and 60 scans, respectively. Data analysis and fitting were performed in the CasaXPS Software. High-resolution spectra were fitted with a 70% Gaussian-30% Lorentzian line shape, and a Shirley background was applied. The binding energy scale was adjusted by assigning the signal of graphitic carbon to 285 eV. The FWHM for the N peaks was fixed between 1.5 and 1.6, and the spectra were fitted based on previously established protocols for similar materials.

X-Ray Absorption Spectroscopy (XAS): Operando XAS measurements in QXAFS mode were performed at P64 beamline[60,61] at PETRA III synchrotron (Hamburg, Germany), and at ROCK beamline[62] at SAMBA synchrotron (Paris, France). XAS measurements were performed in fluorescence mode at Cu K-edge (8979 eV).

At both beamlines, a channel-cut Si(111) quick-scanning monochromator oscillating with a 1 Hz frequency was used for energy selection. Each 6 collected spectra were further averaged, limiting the time resolution of the experiment to 6 s per spectrum. An ionization chamber filled with nitrogen was used to measure the intensity of incoming X-rays. Fluorescence signal intensity was measured using a PIPS detector.

Data alignment at the ROCK beamline was done by aligning the glitches in the experimental data with those in the spectrum for a reference Cu foil. At the P64 beamline, the alignment was done by collecting the spectrum of the Cu foil at the beginning of each QXAFS scan, before the sample was moved into the beam. Data extraction and first averaging were done using dedicated beamline-specific software. Further processing of QXAFS datasets was done using a series of in-house built Wolfram Mathematica scripts. For EXAFS data fitting, the same approach was used as discussed in the recent work,[39] but with a reduced *k*-range used for EXAFS fitting (between 3.0 and 8.0 Å^{-1}) due to the lower signal-to-noise ratio in our QXAFS data.

For the *operando* experiments, the samples were spray-coated on a carbon electrode and mounted in the in-house-built single-compartment electrochemical cell.[63] The working carbon electrode acted simultaneously as a window for the incoming X-ray photons and emitted X-ray fluorescence. A Pt mesh was used as a counter electrode. As a reference electrode, a leak-free Ag/AgCl electrode was used. CO_2-saturated 0.1 M $KHCO_3$ solution was used as an electrolyte. CO_2 was continuously bubbled through the electrolyte during the experiment. Furthermore, a peristaltic pump maintained a continuous electrolyte flow. A BioLogic potentiostat was used to control the applied potential.

X-Ray Emission Spectroscopy (vtc-XES) and High-Resolution Fluorescence Detected XANES (HERFD-XANES): Operando valence-to-core X-ray emission spectroscopy (vtc-XES) of Cu Kβ"" and K$\beta_{2,5}$ lines, and Cu Kβ high-energy resolution fluorescence detected X-ray absorption near edge structure (HERFD-XANES) measurements were performed at ID26 beamline at ESRF synchrotron (Grenoble, France).[64] The storage ring operated in 7/8 multi-bunch mode with an electron current of 200 mA. The incident radiation was generated by three undulators and monochromatized using a pair of cryogenically cooled Si(111) crystals. The energy calibration of the incident beam was performed with a metallic Cu foil reference, setting the first inflection point of the Cu K-edge at 8979 eV. HERFD-XANES spectra were acquired in continuous scan mode, by varying the incident energy from 8970 to 9070 eV across the Cu K-edge, with an energy step of 0.1 eV and an acquisition time of ≈40 s per spectrum. Only photons corresponding to the maximum intensity of the Cu K$\beta_{1,3}$ emission line (≈8906 eV) were detected. This energy selection was achieved using the (800) reflection of a Ge (100) analyser crystal configured in a vertical Rowland geometry.[65] The crystal was spherically bent according to the Johann geometry to focus the fluorescence radiation onto an APD detector (200 µm thickness, 10 × 10 mm^2 active area). To mitigate the potential beam-induced damage, the beam position on the sample was shifted after each scan.[66] For each step in the experimental protocol, ≈30 spectra were acquired and merged. Normalization of HERFD-XANES data was carried out using the ATHENA code.[67]

For vtc-XES measurements, the energy of incident X-rays was fixed at 9200 eV. The X-ray emission scans were performed using the same analyzer crystal as for the HERFD-XANES, acquiring the signal between 8915 and 9000 eV. Each XES spectrum was acquired for ≈30 min, and three spectra per condition were collected and subsequently merged during the post-processing. For the vtc-XES spectra, the background subtraction was carried out by fitting the high-energy tail of the K$\beta_{1,3}$ line with a Voigt profile and subtracting it. The resulting background-free vtc-XES profiles were then normalized by their area.

Operando vtc-XAES and HERFD-XANES measurements were performed using the same electrochemical cell as used for QXAFS measurements, positioned at a 45° angle with respect to the incident X-ray beam.

Supporting Information

Supporting Information is available from the Wiley Online Library or from the author.

Acknowledgements

D.H. thanks the funding provided by the Alexander von Humboldt Foundation. The authors acknowledge SOLEIL (Paris, France) and DESY (Hamburg, Germany) for the provision of experimental synchrotron radiation facilities, and the authors would like to thank Dr. Stephanie Belin for assistance in using the beamline "ROCK" at SOLEIL, and Dr. W. Caliebe for assistance in using the P64 beamline of PETRA III at DESY. The authors also acknowledged the ESRF synchrotron facility for the allocation of beamtime at ID26. The authors are grateful to Dr. Viktoria Saveleva, Luca Bugarin, and Peter Glatzel for the support provided during our experiment at the ID26 beamline. This work was supported by the German Federal Ministry of Education and Research (Bundesministerium für Bildung und Forschung, BMBF) under Grant No. 03EW0015B (CatLab) and the Deutsche Forschungsgemeinschaft (DFG, German Research Foundation) under Germany´s Excellence Strategy – EXC 2008 – 390540038 – UniSysCat.

Open access funding enabled and organized by Projekt DEAL.

Conflict of Interest

The authors declare no conflict of interest.

Author Contributions

D.H. conceptualization, data curation, investigation, methodology, visualization, writing-original draft. J.T. data curation, investigation, methodology, visualization, writing-original draft. A.M. data curation, investigation. H.S.J data curation, investigation. E.O. data curation, investigation, visualization. M.R. data curation, investigation. A.B. data curation, investigation. A.Y. data curation, investigation. U.H. data curation, investigation. A.H. data curation, investigation. C.R. data curation, investigation. F.T.H data curation, investigation. P.G. data curation, investigation. B.R.C. conceptualization, supervision, writing- review & editing.

Data Availability Statement

The data that support the findings of this study are available from the corresponding author upon reasonable request.

Keywords

C_{2+} products, cluster formation, metal-nitrogen doped carbon, potential dependence, pulsed CO_2 reduction, singly dispersed copper

Received: April 29, 2025
Revised: June 17, 2025
Published online: August 4, 2025

[1] D. Gao, R. M. Arán-Ais, H. S. Jeon, B. R. Cuenya, *Nat. Catal.* **2019**, *2*, 198.
[2] W. Ma, S. Xie, T. Liu, Q. Fan, J. Ye, F. Sun, Z. Jiang, Q. Zhang, J. Cheng, Y. Wang, *Nat. Catal.* **2020**, *3*, 478.
[3] B. Endrődi, G. Bencsik, F. Darvas, R. Jones, K. Rajeshwar, C. Janáky, *Prog. Energy Combust. Sci.* **2017**, *62*, 133.
[4] B. Belsa, L. Xia, F. P. García de Arquer, *ACS Energy Lett.* **2024**, *9*, 4293.
[5] X. Lu, D. Y. C. Leung, H. Wang, J. Xuan, *Appl. Energy* **2017**, *194*, 549.
[6] B. Endrődi, E. Kecsenovity, A. Samu, T. Halmágyi, S. Rojas-Carbonell, L. Wang, Y. Yan, C. Janáky, *Energy Environ. Sci.* **2020**, *13*, 4098.
[7] I. Grigioni, L. K. Sagar, Y. C. Li, G. Lee, Y. Yan, K. Bertens, R. K. Miao, X. Wang, J. Abed, D. H. Won, F. P. García de Arquer, A. H. Ip, D. Sinton, E. H. Sargent, *ACS Energy Lett.* **2021**, *6*, 79.
[8] S. Nitopi, E. Bertheussen, S. B. Scott, X. Liu, A. K. Engstfeld, S. Horch, B. Seger, I. E. L. Stephens, K. Chan, C. Hahn, J. K. Nørskov, T. F. Jaramillo, I. Chorkendorff, *Chem. Rev.* **2019**, *119*, 7610.
[9] T. Alerte, J. P. Edwards, C. M. Gabardo, C. P. O'Brien, A. Gaona, J. Wicks, A. Obradović, A. Sarkar, S. A. Jaffer, H. L. MacLean, D. Sinton, E. H. Sargent, *ACS Energy Lett.* **2021**, *6*, 4405.
[10] Y. Hori, in *Modern Aspects of Electrochemistry* (Eds: C. G. Vayenas, R. E. White, M. E. Gamboa-Aldeco), Springer, New York, USA, **2008**, pp. 89–189.
[11] G. Zhang, Z.-J. Zhao, D. Cheng, H. Li, J. Yu, Q. Wang, H. Gao, J. Guo, H. Wang, G. A. Ozin, T. Wang, J. Gong, *Nat. Commun.* **2021**, *12*, 5745.
[12] W. J. Durand, A. A. Peterson, F. Studt, F. Abild-Pedersen, J. K. Nørskov, *Surf. Sci.* **2011**, *605*, 1354.
[13] H. Mistry, A. S. Varela, C. S. Bonifacio, I. Zegkinoglou, I. Sinev, Y.-W. Choi, K. Kisslinger, E. A. Stach, J. C. Yang, P. Strasser, B. R. Cuenya, *Nat. Commun.* **2016**, *7*, 12123.
[14] A. M. Ismail, E. Csapó, C. Janáky, *Electrochim. Acta* **2019**, *313*, 171.
[15] S. Verma, X. Lu, S. Ma, R. I. Masel, P. J. A. Kenis, *Phys. Chem. Chem. Phys.* **2016**, *18*, 7075.
[16] D. Gao, F. Scholten, B. R. Cuenya, *ACS Catal.* **2017**, *7*, 5112.
[17] J. C. Bui, C. Kim, A. Z. Weber, A. T. Bell, *ACS Energy Lett.* **2021**, *6*, 1181.
[18] K. W. Kimura, K. E. Fritz, J. Kim, J. Suntivich, H. D. Abruña, T. Hanrath, *ChemSusChem* **2018**, *11*, 1781.
[19] R. Shiratsuchi, Y. Aikoh, G. Nogami, *J. Electrochem. Soc.* **1993**, *140*, 3479.
[20] J. Lee, Y. Tak, *Electrochim. Acta* **2001**, *46*, 3015.
[21] R. M. Arán-Ais, F. Scholten, S. Kunze, R. Rizo, B. R. Cuenya, *Nat. Energy* **2020**, *5*, 317.
[22] C. Kim, L.-C. Weng, A. T. Bell, *ACS Catal.* **2020**, *10*, 12403.
[23] R. Casebolt, K. Levine, J. Suntivich, T. Hanrath, *Joule* **2021**, *5*, 1987.
[24] J. Timoshenko, C. Rettenmaier, D. Hursán, M. Rüscher, E. Ortega, A. Herzog, T. Wagner, A. Bergmann, U. Hejral, A. Yoon, A. Martini, E. Liberra, M. C. de, O. Monteiro, B. R. Cuenya, *Nat. Commun.* **2024**, *15*, 6111.
[25] M. S. Chandrasekar, M. Pushpavanam, *Electrochim. Acta* **2008**, *53*, 3313.
[26] H. S. Jeon, J. Timoshenko, C. Rettenmaier, A. Herzog, A. Yoon, S. W. Chee, S. Oener, U. Hejral, F. T. Haase, B. R. Cuenya, *J. Am. Chem. Soc.* **2021**, *143*, 7578.
[27] J. Timoshenko, A. Bergmann, C. Rettenmaier, A. Herzog, R. M. Arán-Ais, H. S. Jeon, F. T. Haase, U. Hejral, P. Grosse, S. Kühl, E. M. Davis, J. Tian, O. Magnussen, B. R. Cuenya, *Nat. Catal.* **2022**, *5*, 259.
[28] R. C. DiDomenico, T. Hanrath, *ACS Energy Lett.* **2022**, *7*, 292.
[29] A. Herzog, M. L. Luna, H. S. Jeon, C. Rettenmaier, P. Grosse, A. Bergmann, B. R. Cuenya, *Nat. Commun.* **2024**, *15*, 3986.
[30] Y. Xu, J. P. Edwards, S. Liu, R. K. Miao, J. E. Huang, C. M. Gabardo, C. P. O'Brien, J. Li, E. H. Sargent, D. Sinton, *ACS Energy Lett.* **2021**, *6*, 809.
[31] C. W. Lee, N. H. Cho, K. T. Nam, Y. J. Hwang, B. K. Min, *Nat. Commun.* **2019**, *10*, 3919.
[32] D. Karapinar, N. T. Huan, N. Ranjbar Sahraie, J. Li, D. Wakerley, N. Touati, S. Zanna, D. Taverna, L. H. Galvão Tizei, A. Zitolo, F. Jaouen, V. Mougel, M. Fontecave, *Angew. Chem., Int. Ed.* **2019**, *58*, 15098.
[33] J. Li, P. Pršlja, T. Shinagawa, A. J. Martín Fernández, F. Krumeich, K. Artyushkova, P. Atanassov, A. Zitolo, Y. Zhou, R. García-Muelas, N. López, J. Pérez-Ramírez, F. Jaouen, *ACS Catal.* **2019**, *9*, 10426.
[34] W. Ju, A. Bagger, G.-P. Hao, A. S. Varela, I. Sinev, V. Bon, B. Roldan Cuenya, S. Kaskel, J. Rossmeisl, P. Strasser, *Nat. Commun.* **2017**, *8*, 944.
[35] D. Gao, T. Liu, G. Wang, X. Bao, *ACS Energy Lett.* **2021**, *6*, 713.
[36] N. Leonard, W. Ju, I. Sinev, J. Steinberg, F. Luo, A. S. Varela, B. Roldan Cuenya, P. Strasser, *Chem. Sci.* **2018**, *9*, 5064.
[37] L. Ma, W. Hu, B. Mei, H. Liu, B. Yuan, J. Zang, T. Chen, L. Zou, Z. Zou, B. Yang, Y. Yu, J. Ma, Z. Jiang, K. Wen, H. Yang, *ACS Catal.* **2020**, *10*, 4534.
[38] H. Xu, D. Rebollar, H. He, L. Chong, Y. Liu, C. Liu, C.-J. Sun, T. Li, J. V Muntean, R. E. Winans, D.-J. Liu, T. Xu, *Nat. Energy* **2020**, *5*, 623.
[39] D. Hursán, J. Timoshenko, E. Ortega, H. S. Jeon, M. Rüscher, A. Herzog, C. Rettenmaier, S. W. Chee, B. R. Cuenya, *Adv. Mater.* **2024**, *36*, 2307809.
[40] E. Boutin, A. Salamé, M. Robert, *Nat. Commun.* **2022**, *13*, 4190.
[41] X. Bai, X. Zhao, Y. Zhang, C. Ling, Y. Zhou, J. Wang, Y. Liu, *J. Am. Chem. Soc.* **2022**, *144*, 17140.
[42] Z. Weng, Y. Wu, M. Wang, J. Jiang, K. Yang, S. Huo, X.-F. Wang, Q. Ma, G. W. Brudvig, V. S. Batista, Y. Liang, Z. Feng, H. Wang, *Nat. Commun.* **2018**, *9*, 415.
[43] D. Ren, J. Fong, B. S. Yeo, *Nat. Commun.* **2018**, *9*, 925.
[44] K. Artyushkova, *J. Vac. Sci. Technol. A* **2020**, *38*, 31002.
[45] K. F. Ortega, R. Arrigo, B. Frank, R. Schlögl, A. Trunschke, *Chem. Mater.* **2016**, *28*, 6826.
[46] S. Ott, F. Du, M. L. Luna, T. A. Dao, S. Selve, B. R. Cuenya, A. Orfanidi, P. Strasser, *Appl. Catal. B Environ.* **2022**, *306*, 121118.
[47] I. Matanovic, K. Artyushkova, M. B. Strand, M. J. Dzara, S. Pylypenko, P. Atanassov, *J. Phys. Chem. C* **2016**, *120*, 29225.
[48] F. Späth, W. Zhao, C. Gleichweit, K. Gotterbarm, U. Bauer, O. Höfert, H.-P. Steinrück, C. Papp, *Surf. Sci.* **2015**, *634*, 89.
[49] J. Wang, C.-S. Hsu, T.-S. Wu, T.-S. Chan, N.-T. Suen, J.-F. Lee, H. M. Chen, *Nat. Commun.* **2023**, *14*, 6576.
[50] J. R. Vegelius, K. O. Kvashnina, M. Klintenberg, I. L. Soroka, S. M. Butorin, *J. Anal. At. Spectrom.* **2012**, *27*, 1882.
[51] V. A. Saveleva, M. Retegan, K. Kumar, F. Maillard, P. Glatzel, *J. Mater. Chem. A* **2023**, *11*, 18862.
[52] A. Y. Molokova, E. Borfecchia, A. Martini, I. A. Pankin, C. Atzori, O. Mathon, S. Bordiga, F. Wen, P. N. R. Vennestrøm, G. Berlier, T. V. W. Janssens, K. A. Lomachenko, *JACS Au* **2022**, *2*, 787.
[53] E. Gallo, C. Lamberti, P. Glatzel, *Phys. Chem. Chem. Phys.* **2011**, *13*, 19409.
[54] J. Timoshenko, A. Halder, B. Yang, S. Seifert, M. J. Pellin, S. Vajda, A. I. Frenkel, *J. Phys. Chem. C* **2018**, *122*, 21686.

[55] K. Ye, T.-W. Jiang, H. D. Jung, P. Shen, S. M. Jang, Z. Weng, S. Back, W.-B. Cai, K. Jiang, *Nat. Commun.* **2024**, *15*, 9781.
[56] Y. Xu, F. Li, A. Xu, J. P. Edwards, S.-F. Hung, C. M. Gabardo, C. P. O'Brien, S. Liu, X. Wang, Y. Li, J. Wicks, R. K. Miao, Y. Liu, J. Li, J. E. Huang, J. Abed, Y. Wang, E. H. Sargent, D. Sinton, *Nat. Commun.* **2021**, *12*, 2932.
[57] R. Reske, H. Mistry, F. Behafarid, B. Roldan Cuenya, P. Strasser, *J. Am. Chem. Soc.* **2014**, *136*, 6978.
[58] H. Wang, Y. Hao, Y. Sun, J. Pan, F. Hu, D. Kai, S. Peng, *Catal. Lett.* **2023**, *153*, 215
[59] W. Rong, H. Zou, W. Zang, S. Xi, S. Wei, B. Long, J. Hu, Y. Ji, L. Duan, *Angew. Chem., Int. Ed.* **2021**, *60*, 466.
[60] W. A. Caliebe, V. Murzin, A. Kalinko, M. Görlitz, *AIP Conf. Proc.* **2019**, *2054*, 60031.
[61] B. Bornmann, J. Kläs, O. Müller, D. Lützenkirchen-Hecht, R. Frahm, *AIP Conf. Proc.* **2019**, *2054*, 40008.
[62] V. Briois, C. La Fontaine, S. Belin, L. Barthe, T. Moreno, V. Pinty, A. Carcy, R. Girardot, E. Fonda, *J. Phys. Conf. Ser.* **2016**, *712*, 12149.
[63] J. Timoshenko, B. R. Cuenya, *Chem. Rev.* **2021**, *121*, 882.
[64] P. Glatzel, A. Harris, P. Marion, M. Sikora, T.-C. Weng, C. Guilloud, S. Lafuerza, M. Rovezzi, B. Detlefs, L. Ducotté, *J. Synchrotron Radiat.* **2021**, *28*, 362.
[65] K. A. Lomachenko, E. Borfecchia, C. Negri, G. Berlier, C. Lamberti, P. Beato, H. Falsig, S. Bordiga, *J. Am. Chem. Soc.* **2016**, *138*, 12025.
[66] A. Martini, J. Timoshenko, P. Grosse, C. Rettenmaier, D. Hursán, G. Deplano, H. S. Jeon, A. Bergmann, B. R. Cuenya, *Phys. Rev. Lett.* **2024**, *133*, 228001.
[67] B. Ravel, M. Newville, *J. Synchrotron Radiat.* **2005**, *12*, 537.